iScience

CellPress
OPEN ACCESS

Article

Atomically confined calcium in nitrogen-doped graphene as an efficient heterogeneous catalyst for hydrogen evolution

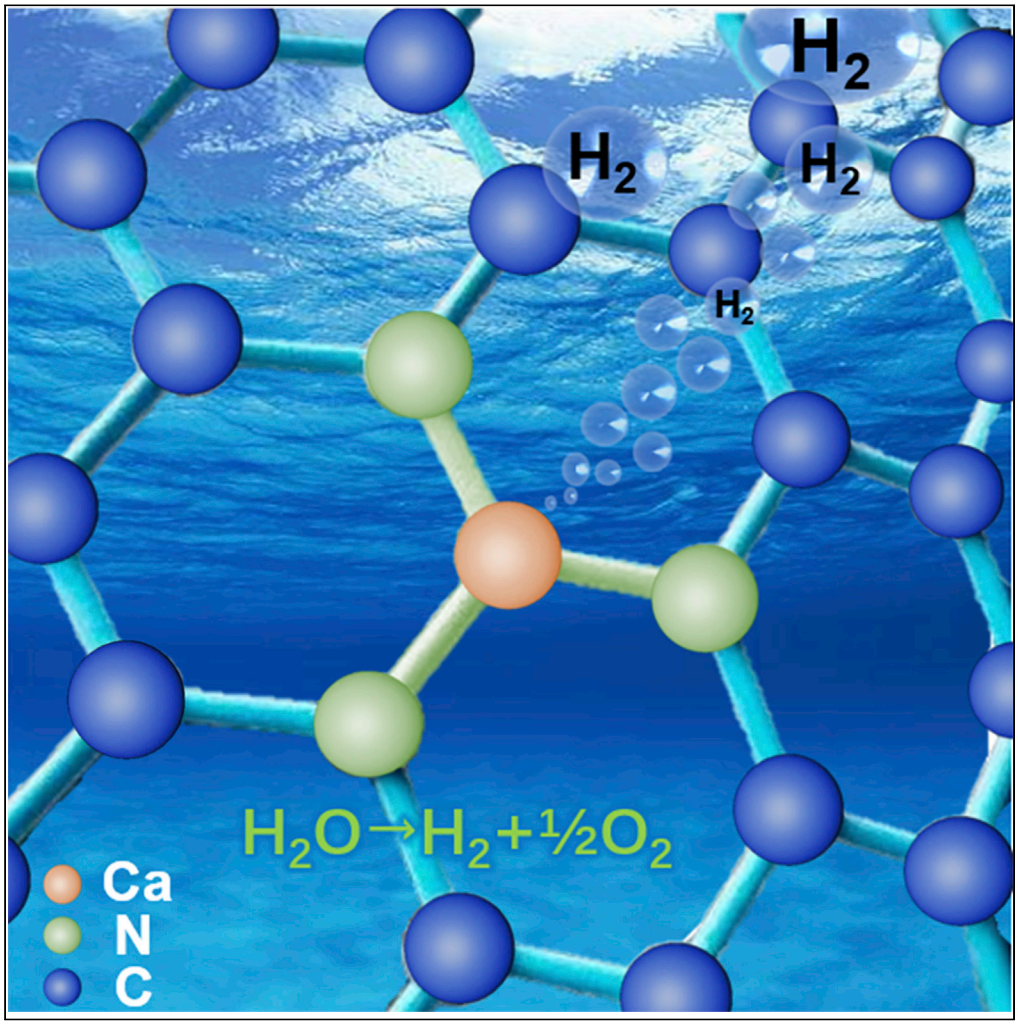

Jie Sun, Suchun Li, Qi Zhao, ..., Wei Chen, Qunjie Xu, Weifeng Yao

yaoweifeng@shiep.edu.cn

Highlights

Atomically confined Ca in nitrogen doped graphene is active and robust for HER

Ca_1-NG has multiple H adsorption configurations with favorable ΔG_{H^*} values for HER

Single Ca atoms are trapped in SV+3N and DV+4N centers, and Ca clustering is prevented

The AQE of the optimal Ca_1-NG/CdS photocatalysts for HER is 57.5% at 420 nm

Sun et al., iScience *24*, 102728
July 23, 2021
https://doi.org/10.1016/j.isci.2021.102728

iScience

CellPress
OPEN ACCESS

Article

Atomically confined calcium in nitrogen-doped graphene as an efficient heterogeneous catalyst for hydrogen evolution

Jie Sun,[1,7] Suchun Li,[2,7] Qi Zhao,[1,6,7] Cunping Huang,[3] Qiang Wu,[1] Wei Chen,[2] Qunjie Xu,[1,4,5] and Weifeng Yao[1,4,5,8,*]

SUMMARY

Calcium is one of the most abundant and cheapest elements on earth. However, due to the lack of d-orbitals for chemical adsorption, it is generally considered as a stoichiometric reagent with no catalytic activities in heterogeneous catalysis. In this research, we have revealed that atomically confined Ca in nitrogen-doped graphene (Ca_1-NG) can be an effective heterogeneous catalyst to boost both electrocatalytic and photocatalytic hydrogen evolution reactions (HER). Ca single atoms anchored in NG can efficiently enhance the HER performance due to the improvement of the interfacial charge transfer rate and suppression of the photo-generated charge recombination. Density functional theory calculations show that the high catalytic activity of Ca_1-NG results from the Ca single atoms in NG, which leads to multiple H adsorption configurations with favorable ΔG_{H^*} values for HER. This research can be valuable for the designing of environmentally friendly, economical and efficient catalysts for renewable hydrogen production.

INTRODUCTION

Calcium (Ca) is the fifth richest element in the Earth's crust. It is one of the cheapest and most biocompatible metals, with high content in the human body. The price of Ca is close to three millionths of the price of noble metal Pt of the same quality (Hill et al., 2016). Like other alkaline earth metals, calcium has, in its outermost S orbital, two valence electrons which are easily given up in chemical reactions. Therefore, calcium is usually bivalent in its compounds and exists in ionic forms. The application of calcium in catalytic reactions could be sustainable, economical and green. However, due to the lack of a d-orbital to enable its oxidation state to change rapidly and reversibly, (a prerequisite for many catalytic cycles) (Harder, 2010; Zhu et al., 2020a, 2020b), calcium metal is generally considered as a stoichiometric reagent with no catalytic performance in heterogeneous catalysts (Gerken et al., 2014; Zhu et al., 2015).

Differing from the rare usage of calcium in heterogeneous catalysis, applications of calcium in homogeneous catalysis have made tremendous progress during the past decade (Hill et al., 2016; Harder, 2010). For example, calcium alkoxide and calcium amide complexes are sufficiently reactive to promote many catalytic reactions. In some cases carbanions, such as benzyl calcium complexes or $(Me_3Si)_2HC$-stabilized alkyl calcium reagents, are highly effective as well. So far, calcium metal complexes have been reported to play a central role in the catalytic cycles of alkenes polymerization (Begouin and Niggemann, 2013), intramolecular hydroamination of aminoalkenes (Crimmin et al., 2005) and hydrosilylation and alkene hydrogenation (Harder and Brettar, 2006). The rapid development of Ca compounds for homogeneous catalysis is mainly based on the viewpoints that the d^0 valence configuration of a Ca^{2+} center in the calcium metal complexes will give it a certain level of 'lanthanide mimetic' characteristics so that a catalytic cycle can be constructed (Hill et al., 2016).

Recently, Zhou and coworkers found that alkaline earth metal elements Ca, Sr, and Ba can form stable octacarbonyl compound molecules which meet the 18-electron rule and exhibit typical transition metal bonding characteristics (Wu et al., 2018). This indicates that the heavy alkaline earth metal elements may behave like transition metals in certain heterogeneous catalytic processes. However, there are few reports on the use of alkaline earth metals for heterogeneous catalysis. For example, Xia et al identified through

[1]Shanghai Key Laboratory of Materials Protection and Advanced Materials in Electric Power, College of Environmental & Chemical Engineering, Shanghai University of Electric Power, No.2588 Changyang Road, Yangpu District, Shanghai, 200090, PR China

[2]Department of Physics and John A. Paulson School of Engineering and Applied Sciences, Harvard University, Cambridge, MA 02138, USA

[3]Aviation Fuels Research Laboratory, Federal Aviation Administration William J. Hughes Technical Center, Atlantic City International Airport, NJ 08405, USA

[4]Shanghai Institute of Pollution Control and Ecological Security, Shanghai 200090, PR China

[5]Shanghai Engineering Research Center of Heat-exchange System and Energy Saving, Shanghai University of Electric Power, Shanghai 200090, PR China

[6]Center of Super-Diamond and Advanced Films (COSDAF) and Department of Chemistry, City University of Hong Kong, Hong Kong SAR, 999077 P. R. China

[7]These authors contributed equally

[8]Lead contact

*Correspondence: yaoweifeng@shiep.edu.cn

https://doi.org/10.1016/j.isci.2021.102728

theoretical calculations that alkaline earth metals, placed in a covalent organic framework, can become effective electrocatalysts for oxygen reduction reaction (ORR), which is the major reaction for hydrogen fuel cells and metal-air batteries (Lin et al., 2017). Chen et al. proved experimentally that Mg, atomically dispersed in the graphene framework, has extremely high ORR activity under both alkaline and acidic conditions (Xu et al., 2019). However, due to the lack of more experimental results, there is still insufficient evidence to show that alkaline earth metals have enough active catalytic sites in heterogeneous catalysis. In addition, the catalytic mechanism of alkaline earth metals in heterogeneous catalytic reactions can be an exciting field for renewable hydrogen production.

Single atom catalysts (SACs) are an innovative type of heterogeneous catalysts in which each isolated active metal atom is fixed on supporting materials (Wang et al., 2019; Kaiser et al., 2020; Zhuo et al., 2020). Although SACs are classified as the heterogeneous catalysts, the presence of single metal atoms in SACs is very similar to that in homogeneous catalysts (Yang et al., 2017). The surface atoms of the supporting materials can be considered as ligand molecules in homogeneous catalysts, which not only stabilize the active metal atoms but also engage in the catalytic reactions (Wang et al., 2019; Wu et al., 2019). The similarity between SACs and homogeneous catalysts has driven us to explore the use of calcium metals for heterogeneous catalytic hydrogen evolution reaction (HER).

In this research, we have found that atomically confined Ca in nitrogen-doped graphene (Ca_1-NG) can be an effective heterogeneous catalyst to boost the electrocatalytic hydrogen evolution (EHE) and photocatalytic hydrogen evolution (PHE) reactions. To the best of our knowledge this is the first report that calcium single atoms have been used as catalysts for the HER. The performance of Ca_1-NG loaded CdS is comparable to that of noble metal Pt loaded CdS for PHE under the same experimental conditions. Density functional theory (DFT) calculations have shown that the excellent performance of Ca_1-NG can be attributed to the optimal adsorption capacity of hydrogen atoms on the Ca-doped active centers.

RESULTS AND DISCUSSION

Synthesis and characterizations of Ca_1-NG

Ca_1-NG was prepared using a facile method previously described for the preparation of Co_1-NG and Ni_1-NG (Zhao et al., 2017; Zhao et al., 2018; Fei et al., 2015). Briefly, a complete mixture of graphene oxide (GO) and $CaCl_2$ was thermochemically treated in an NH_3 atmosphere to form the Ca_1-NG. During this process GO was reduced to NG (supplemental information Figure S1), and the N dopants were incorporated into the graphene lattice to form a strong interaction with metal atoms (Wang et al., 2019; Zhao et al., 2017).

No diffraction peaks of Ca oxides or carbides were detected in the X-ray diffraction (XRD) patterns of Ca_1-NG samples (supplemental information, Figure S1). Transmission electron microscopy (TEM) images show that there are no Ca-related nanoparticles in the prepared Ca_1-NG samples (Figure 1A). However, the energy-dispersive X-ray elemental mapping spectroscopy (EDS) indicated that Ca, N, and C elements are distributed evenly on the prepared Ca_1-NG (Figure 1D). The aberration-corrected high-angle annular dark-field scanning transmission electron microscopy (HAADF-STEM) images of Ca_1-NG further demonstrated that Ca species were homogeneously dispersed in the substrates. As shown in Figures 1B and 1C, a small number of bright spots with diameters less than 0.2 nm are well dispersed on the substrates. The absence of Ca clusters has been confirmed with careful examination at several randomly picked locations during HAADF-STEM observations. These results indicate that all Ca species are atomically dispersed in the Ca_1-NG. The loading content of Ca in Ca_1-NG is 0.52 wt.% based on the analysis of inductively coupled plasma optical emission spectrometer (ICP-OES).

X-ray photoelectron spectroscopy (XPS) analysis was performed to investigate the chemical composition and valence state of Ca_1-NG (Figure 2 and Table S1). The survey spectrum with major C peaks and some smaller peaks of N, O and Ca confirms the presence of C, N, O and Ca in Ca_1-NG (Figure 2A). The high-resolution N 1s spectrum shows that Ca_1-NG catalyst contains mainly pyridinic N (398.0 eV) as well as a small amount of pyrrolic (399.5 eV), graphitic (400.8 eV), and oxidized N species (402.1 eV) (Figure 2B). The presence of pyridinic N is not only favorable for hydrogen evolution activity of Ca_1-NG but also serves as anchoring sites for single metal atoms. Figure 2C shows the high-resolution Ca 2p spectrum of Ca_1-NG. According to the National Institute of Standards and Technology XPS database (Naumkin et al., 2012), the 347.2 eV and 350.8 eV binding energy peaks can be attributed to Ca $2p_{3/2}$ and Ca $2p_{1/2}$, respectively. The absence of metallic Ca $2p_{3/2}$ spectrum (344.9 eV) indicates that the scattered Ca species (shown in

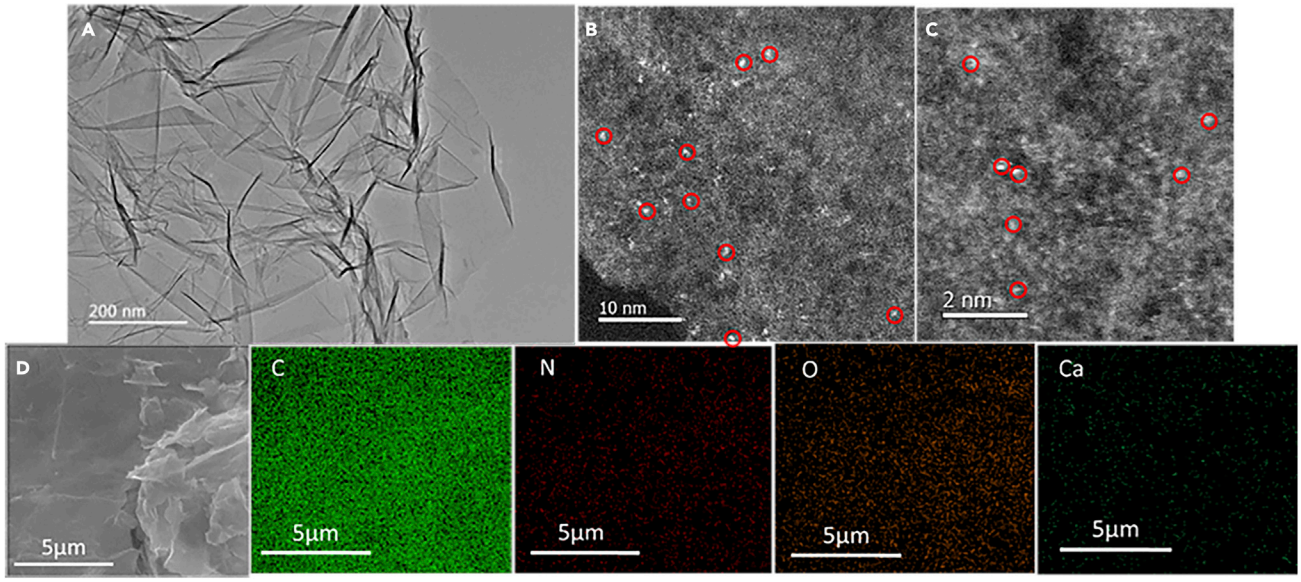

Figure 1. Morphology characterization of Ca_1-NG

(A–C) (A) TEM image and (B and C) HAADF-STEM images of Ca_1-NG nanosheets with scale bars of 10 nm and 2 nm, respectively.

(D) SEM image and selected area energy dispersive X-ray elemental mapping spectroscopy (EDS) for carbon (C), nitrogen (N), oxygen (O), and calcium (Ca) in Ca_1-NG.

HAADF-STEM images) in Ca_1-NG are Ca^{2+} cations. The Raman spectra of the resultant catalysts in Figure 2D exhibit a D-band for defected graphite and a G-band for the doubly degenerate zone center E_{2g} mode (Ferrari and Basko, 2013). The intensity ratio of D band to G band (I_D/I_G) for Ca_1-NG (0.98) is close to that of NG (1.03). This result indicates that the dispersion of individual Ca atoms in the NG matrix has little effect on the degree of disorder and structural defects in the NG laminar structure (Zhao et al., 2018).

The atomic dispersion of Ca cations in Ca_1-NG was further confirmed by the X-ray absorption near-edge structure (XANES) spectroscopy and the extended X-ray absorption fine structure (EXAFS) spectroscopy, which are sensitive to the local environment of metal atoms. Figure 3A shows the Ca K-edge of XANES curves of Ca_1-NG and CaO. Usually a metal foil is used for energy calibration. However, because calcium metal is very active in air, the Ca K-edge XANES spectrum of CaO was used as calibration reference material. As shown in Figure 3A, the adsorption edge position of the Ca_1-NG XANES curves is comparable to that of CaO, indicating that Ca metal atoms in Ca_1-NG are in cationic states. This agrees well with the results of the XPS spectra (Figure 2C). Further structural information was obtained from Ca K-edge EXAFS analyses (Table S2). Figures 3B and 3C show the Ca K-edge EXAFS K-space and R-space plots, respectively, for the Ca_1-NG. It is noted that the EXAFS curve of Ca_1-NG is obviously different from that of CaO. The R space plots of Ca_1-NG show a sharp peak at approximately 2.1 Å. However, CaO shows two strong bonding features at around 1.9 Å and 3.1 Å, which are attributed to the Ca-O bond and Ca-O-Ca bonds, respectively. The major peak for Ca_1-NG at approximately 2.1 Å can be corresponded to the formation of Ca-N bond, which is longer than that of Ca-O bond (1.9 Å) in CaO. Atomic structure simulations indicate that the anchored Ca single atoms are located at the defective sites of NG derived from pyridine-N (Figure 3D and supplemental information Figure S2). The fitting results indicated a CN of 2.8 for Ca-N contribution in Ca_1-NG. This result corresponds well to DFT calculations (Figure S17), which indicate that single Ca atoms anchored in pyridinic N defects in graphene are stable (Detailed information can be found in the following DFT calculation section of this research).

Performances for electrocatalytic/photocatalytic HERs

Experimental results have shown that the prepared Ca_1-NG exhibits more enhanced activities for HER under both acidic and weak basic conditions than do other obtained catalysts (Figures 4A and 4B and supplemental information Figure S3). The HER activities of Ca_1-NG were evaluated, both in 0.5 M H_2SO_4 and 1.0 M $(NH_4)_2SO_3$ solutions using a standard three-electrode electrochemical cell. The commercial 20 wt.% Pt/C and the prepared GO and NG were also evaluated as baseline catalysts. All potentials were referenced to

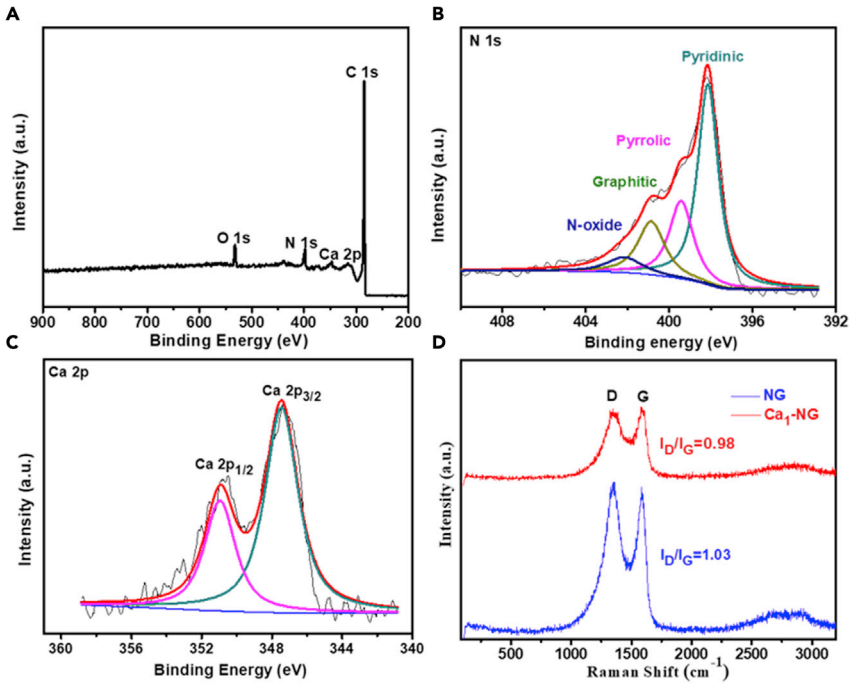

Figure 2. Elemental composition analysis

(A–D) (A) XPS survey spectra and (B) N 1s and (C) Ca 2p high-resolution XPS spectra of Ca_1-NG, and (D) Raman spectra of the synthesized NG and Ca_1-NG.

the reversible hydrogen electrode (RHE) and with iR-corrected. As shown in Figure 4A, Ca_1-NG shows HER activity in acidic solution with an onset potential (E_{onset}) of 21 mV and an overpotential of 151 mV to deliver a current density of 10 mA cm^{-2}. For comparison, NG and GO show poor activities toward HER, requiring much greater overpotentials of 297 mV and 338 mV, respectively, to generate the same 10 mA cm^{-2} current density.

The enhanced HER activity of Ca_1-NG is further confirmed by the smaller Tafel slope of 76 mV dec^{-1} for Ca_1-NG as compared to 137 mV dec^{-1} for NG and 147 mV dec^{-1} for GO (Figure 4B). The small Tafel slope indicates that the rate-determining step of Ca_1-NG is either the electrochemical desorption of H or the discharge reaction, following the Volmer-Heyrovsky mechanism (Dong et al., 2018). Although the Tafel slope of Ca_1-NG is higher than that for the benchmarked 20 wt.% Pt/C catalyst (36 mV dec^{-1}), it is significantly lower than that of NG without Ca single atoms. This result suggests that the new Ca single atom can be effectively used as the catalytically active site of HER. In addition, Ca_1-NG has also shown more favorable HER activity under neutral (or weak basic) conditions of 1.0 M $(NH_4)_2SO_3$ with pH = 8.0, as the obvious shift of the polarization curve for Ca_1-NG catalyst to a lower overpotential (Figure S3). These results indicate that the incorporation of calcium single atoms into N-doped graphene can lead to a profound enhancement of the HER activity for Ca_1-NG under both acidic and weak basic conditions.

The electrochemical active surface area (ECSA) of prepared catalysts was analyzed by means of C_{dl} in Figure S4. The results showed that the capacitances of GO, NG, and Ca_1-NG are 3.07, 3.68, and 5.22 mF cm^{-2} in a 0.5 M H_2SO_4 solution, corresponding to 76.8, 92.0, and 130.5 cm^2 ECSAs, respectively. The ECSA of a 20 wt.% commercial Pt/C catalyst was measured using the underpotential deposition hydrogen (UPD-H) adsorption/desorption voltammetry method, which is usually used for the determination of ECSAs for noble-metal electrocatalysts. As shown in Figure S5, the ECSA for Pt/C was determined to be 285.7 cm^2. The turnover frequencies (TOFs) of the testing catalysts were calculated to evaluate the intrinsic activities of the catalysts. At overpotential of 100 mV, the TOF values of the GO, NG, and Ca_1-NG were 0.125, 0.147, and 1.134 H_2 s^{-1}, respectively. These values revealed that Ca_1-NG had intrinsic HER activity excelling other catalysts. An equivalent circuit simulation for electrochemical impedance spectroscopy (EIS) tests was carried out from 10^{-2} Hz–10^6 Hz (Figure S6). Ca_1-NG shows a smaller arc

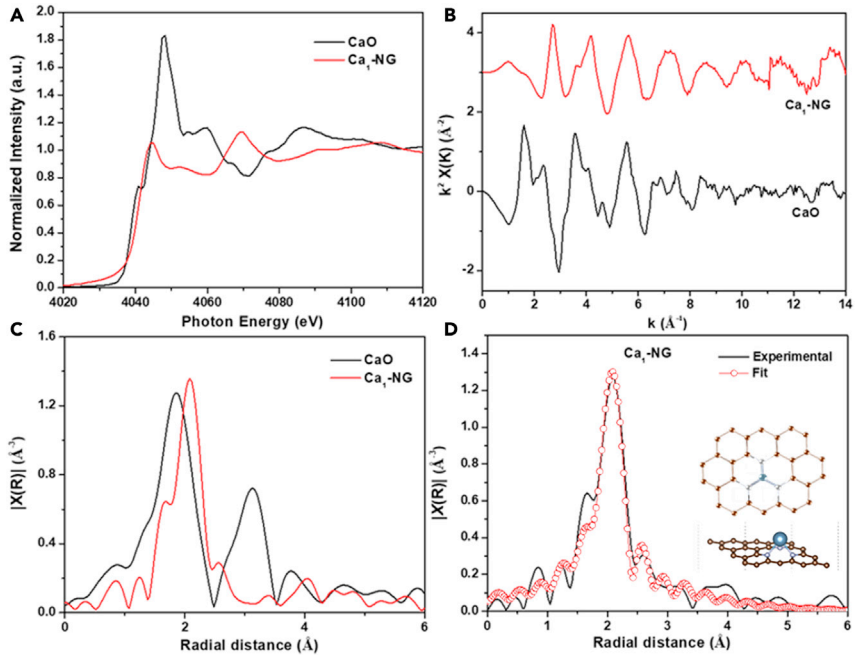

Figure 3. Structure characterization of Ca_1-NG

X-ray absorption characterization.

(A–C) (A) XANES and (B and C) Ca K-edge FT-EXAFS spectra of Ca_1-NG and the reference samples at k-space and R-space, respectively.

(D) The corresponding Ca K-edge EXAFS fitting curves for Ca_1-NG at R-space. The insets of (D) are the schematic models of Ca_1-NG. Atom colors: royal blue, Ca; brownish yellow, C; dark gray, N.

radius compared to those of GO and NG, which means that the electrochemical impedance of Ca_1-NG is smaller than those of GO and NG.

Electrochemical stability is an important indicator used to evaluate the catalytic performance of catalysts. The result of the i-t curve (Figure S7) shows that the catalytic current remains constant at about 17 mA cm^{-2} at 200 mV for over 30,000 s. This result indicates the high stability of Ca_1-NG catalyst in a 0.5 M H_2SO_4 solution. The XPS and STEM analyses of Ca_1-NG after HER are shown in Figures S8 and S9. The results show that the XPS and STEM characterizations of Ca_1-NG do not change significantly after the reaction, proving that the structure of Ca_1-NG is stable.

On the other hand, the prepared Ca_1-NG can significantly enhance the performance of CdS for PHE. The formation of the Ca_1-NG loaded CdS composite photocatalysts (Ca_1-NG/CdS) was confirmed via TEM images (Figure S10). XRD patterns and UV-visible light absorption spectra show that a small amount of Ca_1-NG loading does not affect the crystal structure of CdS but significantly improves the light absorption capacity of the photocatalyst (Figures S11 and S12). The PHE performance of Ca_1-NG/CdS under visible light irradiation at 420 nm was evaluated using $(NH_4)_2SO_3$ as an electron donor. As shown in Figures 4C and 4D, Ca_1-NG/CdS exhibits much higher PHE activities compared to bare CdS and NG loaded CdS. The rate of hydrogen evolution for 0.5 wt.% Ca_1-NG/CdS (92.0 μmol/h) is 8.1 times greater than that of bare CdS (11.3 μmol/h) and 1.6 times greater than that of 0.5 wt.% NG/CdS photocatalyst (57.7 μmol/h). Moreover, the catalytic performance of 0.5 wt% Ca_1-NG/CdS was comparable to that of 0.5 wt.% Pt/CdS (Figure S13), an active photocatalyst for PHE. In order to verify the role of CaO nanoclusters in hydrogen production we loaded CaO onto the surface of NG and successfully prepared CaO-NG/CdS. The hydrogen evolution performance of CaO-NG/CdS is shown in Figure S14. It is noted that CaO nanoclusters have no catalytic effect on the HER. Therefore, we can conclude that it is the Ca single atoms in Ca_1-NG/CdS that play a major catalytic role, rather than the CaO nanoclusters. It is noted that the loading content of Ca in Ca_1-NG is only 0.52 wt.% (based on ICP-OES analysis). That means that very few Ca atoms, only 26 parts per million mass of CdS, are needed in order to facilitate the PHE reactions. This result also indicates that single

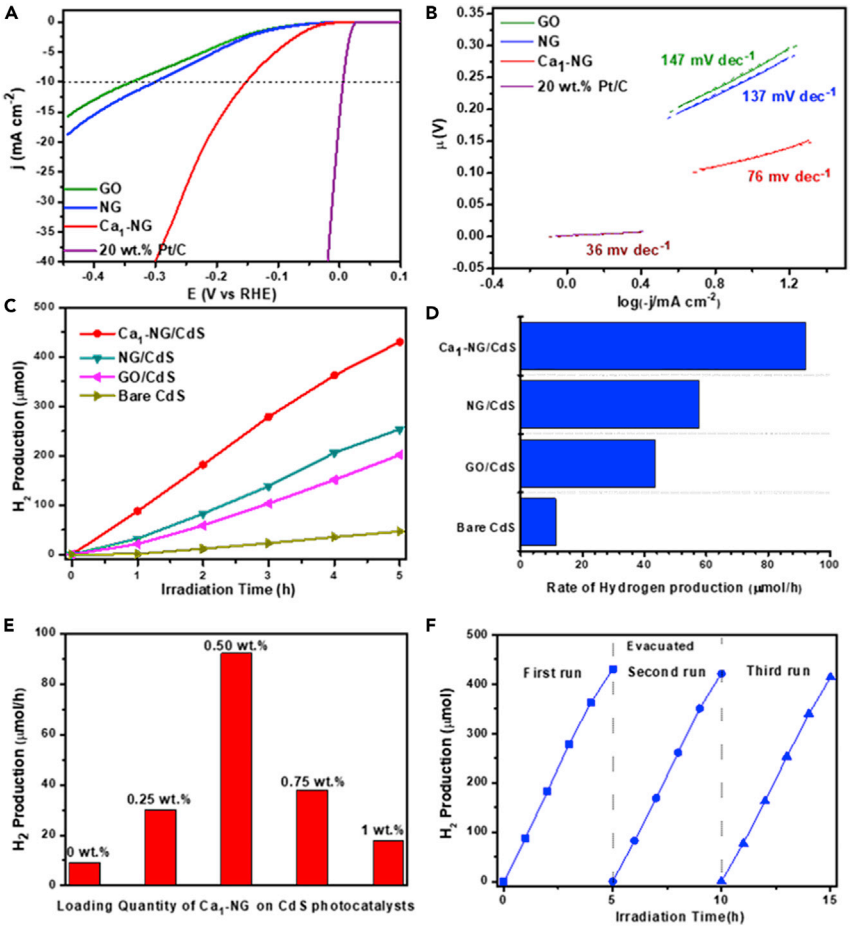

Figure 4. Hydrogen evolution performance

(A and B) (A) Polarization curves and (B) Tafel plots for HER from a 0.5 M H_2SO_4 solution of the modified GCEs comprised of GO, NG, Ca_1-NG and commercial Pt/C electrocatalysts. The catalyst loading density is 0.38 mg cm^{-2}.

(C and D) (C) Photocatalytic H_2 evolution and (D) Specific photocatalytic H_2 evolution rates of pure CdS, 0.5 wt.% GO/CdS, 0.5 wt.% NG/CdS and 0.5 wt.% Ca_1-NG/CdS.

(E) Hydrogen production rates of Ca_1-NG/CdS with various Ca_1-NG mass loading percents.

(F) Catalyst lifespan tests over 0.5 wt.% Ca_1-NG/CdS.

calcium atoms in NG play an important role in the improvement of the hydrogen evolution activity, which agrees well with the enhanced EHE performance for Ca_1-NG.

The effect of Ca_1-NG loading concentration was investigated and the results are shown in Figure 4E. The rate of hydrogen evolution increases from 11.3 μmol/h to 92 μmol/h as the Ca_1-NG loading on CdS photocatalysts increases from 0.0 to 0.5 wt.%. Further increasing Ca_1-NG loading, however, results in a significant drop in the rate of hydrogen evolution. This decline is possibly due to the light blockage effect of Ca_1-NG on the surface of CdS. The optimal loading of Ca_1-NG on CdS is about 0.5 wt.% under the present reaction conditions. The apparent quantum efficiency of the optimal Ca_1-NG/CdS photocatalysts for hydrogen production is 57.5% at 420 nm wavelength. As illustrated in Table S3, this efficiency (57.5%) is one of the greatest ever reported for non-noble-metal cocatalysts.

The stability of Ca_1-NG/CdS photocatalyst was verified by a three PHE reaction cycles test. As shown in Figure 4F, no significant decrease in the rate of hydrogen evolution was observed during the cyclic test. During the three PHE cycles test a total of 1.264 mmol H_2 was produced. The turnover numbers (TONs), which are defined as the total hydrogen atoms evolved per mole of CdS photocatalyst and per mole of Ca anchored in Ca_1-NG/CdS, are 73 and 779363, respectively. These large TONs indicate that hydrogen is produced

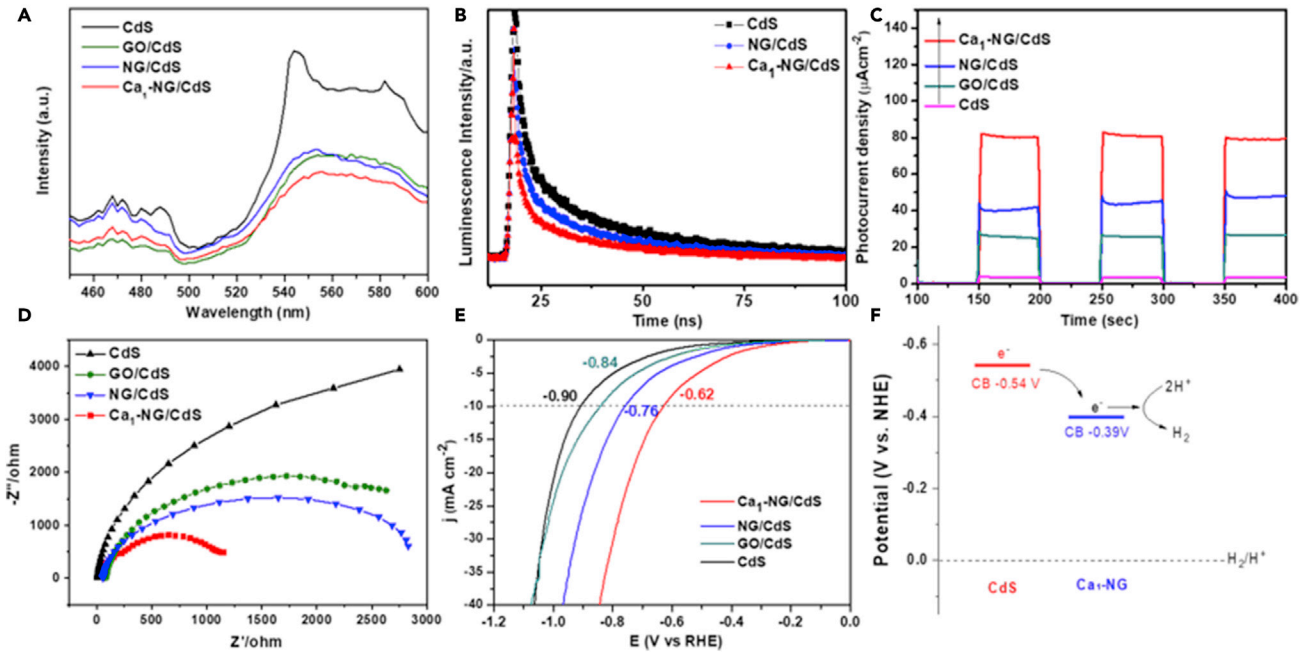

Figure 5. Optical performance and photoelectrochemical performance

(A–E) (A) Steady-state PL spectra, (B) Time-resolved transient PL decay spectra, (C) Photoelectrode transient photocurrent responses, (D) Nyquist plots of EIS and (E) LSV curves of the bare CdS, 0.5 wt. % NG/CdS, 0.5 wt. % GO/CdS and 0.5 wt.% Ca1-NG/CdS photocatalysts, respectively.

(F) Schematic illustration of interfacial charge transfer in Ca1-NG/CdS.

from the photocatalytic reduction of water rather than from the photo-corrosion of either CdS or Ca in the Ca_1-NG/CdS photocatalysts. Additionally, XRD, TEM and ICP tests have shown that there are no significant differences for the Ca_1-NG/CdS photocatalyst before or after the stability test (Figures S10 and S6 and Table S4), indicating that Ca_1-NG/CdS is stable during PHE processes. The stability of Ca_1-NG/CdS was further confirmed by a long-term photoelectrocatalytic test in 0.5 M H_2SO_4. As can be seen in Figure S15, the linear sweep voltammetry (LSV) curves for Ca_1-NG/CdS show no clear difference before or after a long-term photoelectrocatalytic hydrogen evolution test. This result also indicates that Ca_1-NG/CdS is a stable catalyst for PHE.

Charge separation, transfer routes, and efficiency of Ca_1-NG/CdS photocatalyst

Photoluminescence (PL) and time-resolved photoluminescence (TRPL) decay spectra measurements were carried out to evaluate the charge carrier trapping and transfer mechanism in Ca_1-NG/CdS photocatalyst during photocatalytic reactions (Figures 5A and 5B). The weak peak around 475 nm in PL spectra can be ascribed to the band edge emission of CdS, while the higher broad band at around 550 nm originates from the trap states (Veamatahau et al., 2015; Mathew et al., 2011). Clearly, the PL intensity of Ca_1-NG/CdS is much weaker than that of bare CdS, indicating that the photogenerated electron-hole pair recombination is effectively suppressed after Ca_1-NG is loaded onto the surface of CdS. This may result from the effect of co-catalyst trapping photogenerated electrons (Chen et al., 2010). Moreover, the PL intensity of Ca_1-NG/CdS was weaker than those of NG/CdS and GO/CdS. This result is consistent with the better PHE performance for Ca_1-NG/CdS.

The transfer efficiency of photogenerated charge carriers was further confirmed by the TRPL decay spectra (Figure 5B). The decay curves easily approximate a biexponential function. As shown in Table S5, the average lifetime of the PL decay in bare CdS was 2.37 ns. However, after NG and Ca_1-NG loading, the PL lifetimes of the NG/CdS and Ca_1-NG/CdS photocatalysts were reduced to 1.88 and 0.93 ns, respectively. These results suggest that the presence of Ca_1-NG provides a new pathway for the electron transfer from CdS to Ca_1-NG, leading to a significant decrease in the PL decay lifetime (Jiang et al., 2017). In addition, the lower PL average decay lifetime of Ca_1-NG/CdS compared to that of NG/CdS further confirms that Ca single atoms anchored in NG result in more effective separation of the photogenerated carriers, thereby leading to higher photocatalytic activity.

To further understand the role of Ca_1-NG cocatalyst in PHE, the transient photocurrent-time curves of Ca_1-NG/CdS, NG/CdS, GO/CdS and bare CdS samples underwent several on-off cycles of intermittent irradiation at 420 nm. As shown in Figure 5C, all the samples demonstrated a prompt photocurrent generation during the on and off illumination cycles. These on-off cycles also show high reproducibility. It is noteworthy that Ca_1-NG/CdS exhibits greater photocurrent compared to NG/CdS and bare CdS. The photocurrent intensity of Ca_1-NG/CdS was almost two times higher than that of NG/CdS, suggesting the positive roles of Ca doping in the acceleration of charge separation, which agrees with the results shown in Figures 5A and 5B.

From a charge transfer viewpoint, EIS further shows the positive roles of Ca single atoms in Ca_1-NG/CdS for PHE. In this research, EIS was carried out under visible light illumination and using a typical three-electrode setup. A smaller semicircle radius of an EIS curve generally means a lower charge transfer resistance and thus faster interface charge transmission of a photocatalyst (Zheng et al., 2020; Shi et al., 2020; Yao et al., 2019). As shown in Figure 5D, the Nyquist plots of Ca_1-NG/CdS have much smaller semicircles than those of NG/CdS and bare CdS, suggesting a more efficient charge separation and transfer within Ca_1-NG/CdS and, therefore, a better PHE performance.

LSV tests under 420 nm visible light irradiation using 1.0 M $(NH_4)_2SO_4$ aqueous solution as a photolyte show that Ca_1-NG loading can effectively reduce the overpotential of CdS for PHE. As shown in Figure 5E, the overpotential for Ca_1-NG/CdS at -10 mA cm^{-2} is 0.62 V, much lower than those of NG/CdS (-0.76 V) and bare CdS (-0.90 V). (Note that a lower overpotential means a lower required activation energy for the HER ($2H^+(aq) + 2e^- \rightarrow H_2(g)$) (Kweon et al., 2020) and is also favorable for photocatalytic H_2 production (Shi et al., 2020; Yao et al., 2019; Luo et al., 2015)). Additionally, the conduction band (CB) potentials of Ca_1-NG and CdS were estimated to be -0.54 and -0.39 V (vs. NHE) using the Mott-Schottky method (Figure S16). A more negative CB position indicates that photogenerated electrons in CdS under light irradiation can migrate from CdS to Ca_1-NG (Figure 5F), which agrees well with the results of PL and TRPL decay spectra.

We can conclude, based on these characterization results, that Ca_1-NG can serve not only as an electron storage medium to effectively inhibit the recombination of charge carriers, but also as active sites to accelerate the HERs. In addition, single Ca atoms doping in NG plays a key role in the improvement of catalytic performance of Ca_1-NG and Ca_1-NG/CdS for hydrogen evolution.

Catalytic mechanism of Ca single atoms in NG for hydrogen evolution

DFT simulations were carried out to provide an in-depth theoretical understanding of the roles the Ca single-atoms play in the HER and PHE.

Our calculations show that the Ca atom is located on the central axis after structural relaxation (Figures S17), which is consistent with experimental observations (Lin et al., 2015). Both the SV+3N + Ca and DV+4N + Ca structures (two most common carbon vacancies: single vacancy (SV, refer Figure S17A) and double vacancy (DV, refer Figure S17B), exist in the NG. Creation of an SV (DV) leads to three (four) carbon atoms having dangling electrons (CN equals 2). Replacing one of these three/four carbon atoms by N results in a pyridinic-N that coexists with an SV/DV. In principle we can replace multiple carbon atoms to form SV + xN (x = 1, 2, 3) and DV + yN (y = 1, 2, 3, 4) structures, and the Ca atom is about 1.77 Å and 1.30 Å above the 2D plane, forming identical N-Ca bonds with lengths of 2.18 Å and 2.26 Å, respectively (slightly longer N-Ca bonds in the DV+4N + Ca structure indicates weaker N-Ca bonding strength. This is because the two valence electrons of Ca split into only 3 Ca-N bonds in the SV+3N + Ca structure, whereas they have to split into 4 Ca-N bonds in the DV+4N + Ca structure, resulting in less electron density forming each Ca-N bond in the latter case). In a previous study, we found that a Ni single atom could also be supported above the SV+3N structure, but it would drop into the double vacancy surrounded by 4 N, making it no longer useful for HER. Here, a Ca single atom could be supported above the plane for both SV+3N and DV+4N structures, as the size of the Ca atom is larger than most transition metal atoms. The calculated adsorption energies for Ca single atoms adsorbed at the centers of SV+3N and DV+4N structures are $\Delta E_{Ca} = -4.50$ eV and -5.96 eV, respectively. These adsorption energies are much more negative than the Ca crystal cohesive energy of about -1.84 eV (Lee et al., 2009), indicating that the Ca adsorption at the SV+3N and DV+4N centers is extremely stable.

Next, we studied H adsorption on these four structures and examined how the Ca single atom affects the H adsorption energy. We considered H adsorption at both Ca-sites and N-sites (we ignore H adsorption at

the C-sites because they are not stable and are much less affected by the Ca atom). Because each structure involves several N atoms, we denote them as N_1, N_2, N_3 (and N_4), as illustrated in Figure 6. We consider all possible situations, with several H adsorbed onto a combination of Ca and N atoms, and we name an H adsorption configuration by the H adsorption sites. For example, [N_1, N_2, Ca*] denotes a configuration with three H atoms adsorbed onto N_1, N_2, and Ca, respectively. When discussing ΔG_{H^*} values of a particular H within a configuration involving several H, we further denote the adsorption site of the discussed H using *. For instance, in the former example [N_1, N_2, Ca*], the discussed H is on Ca* site. Various H adsorption configurations for the SV+3N versus SV+3N + Ca and DV+4N versus DV+4N + Ca structures are shown in Figures 6 and 7. In particular, for the structures involving Ca, H^+ coming from solution above graphene can adsorb onto the Ca-site, and H^+ from underneath graphene can adsorb onto the N-site. With the same number m (m > 1) of adsorbed H, the catalytic system can have these H atoms (i) all adsorb onto the N-sites (Figure 6B) or (ii) it can have one adsorbed onto Ca and the remaining m-1 H adsorbed onto N-sites (Figures 6C and 7). Although the energies (i) and (ii) might be slightly different, both structures could exist in solution with sufficient lifetime for catalyzing HER. It is difficult to have structural transition from one to the other since H on Ca-site and H on N-site are spatially separated on different sides of graphene. Therefore we considered both structures.

In the case of a single Ni atom supported on SV+3N or DV+4N structures, we find that Ni-N bond could be broken if too many N and Ni sites are adsorbed with H. Here the Ca-N bonds are not broken, even if all the N and Ca sites are adsorbed with an H (Figure 6). This is due to the unique property of Ca, that it can host a large CN (Yoon et al., 2008). This unique property makes the Ca structure extremely stable/robust in the dynamic solution and makes sure all the H adsorption sites can contribute to HER.

Figures 6 and 7 show clearly that with a Ca atom adsorption we get not only an extra Ca-site for H adsorption, but also more than three times as many possible processes for H adsorption. In addition, many of these H adsorption configurations are associated with small $|\Delta G_{H^*}|$ values, as highlighted in bold in Figures 6 and 7.

All H adsorption processes in the four structures and corresponding ΔG_{H^*} values are illustrated in Scheme 1, where ΔG_{H^*} is reflected by the G difference between the initial configuration and final configuration. For the structures without Ca (black curves in Scheme 1), most $|\Delta G_{H^*}|$ values are very large. There is only one small $|\Delta G_{H^*}|$ (0.34eV), when an H is adsorbed to N_2 of the SV+3N [N_1] configuration, as highlighted in red. On the contrary, the two structures with Ca (blue curves in Scheme 1) both involve many $|\Delta G_{H^*}|$ values close to zero, as highlighted by red or orange. In particular, the red processes are especially useful for HER as they not only involve small $|\Delta G_{H^*}|$ values but also start from configurations that are highly likely to exist in the solution, because the starting configurations are either the initial configuration without any H or a configuration requiring a small or even negative ΔG_{H^*} from the initial configuration. The SV+3N and DV+4N structures involve only one red H adsorption process, while the SV+3N + Ca and DV+4N + Ca structures involve 4 red H adsorption processes. In addition, all the red lines H adsorption are on the Ca-site, indicating that the Ca atom plays an essential role in providing many suitable H adsorption configurations to catalyze HER.

Before explaining the detailed mechanism of Ca atoms in HER we first examine the effect of H coverage in the structures without Ca. For both SV+3N and DV+4N structures higher H coverage induces larger ΔG_{H^*} values (Figure 6A), consistent with the general trend that H binding becomes less stable when more H are adsorbed in the vicinity. When H coverage is low (Figure 6A black boxes), the ΔG_{H^*} values are very negative (−2.32 eV, −1.53 eV, and −1.34 eV). (The delta G_H value for the first H* in the SV+3N defect is about 0.8eV more negative than that in the DV+4N defect because the former configuration also involves more interaction between H* and N2, N3 (more details are given in SI), indicating a very strong H binding. Adding one more H to either structure dramatically increases ΔG_{H^*} to quite positive values (0.34 eV and 0.78 eV), indicating a significant reduction in the binding strength of additional H. The abrupt reduction of H binding strength can be understood from their atomic structures. For the three configurations with low H coverages (Figure 6A black boxes) the H atom(s) is located inside the vacancy hole and the whole structure is well within a 2D plane (see side view), where H and N form a sp^2-like bond. In addition, the in-plane H interacts with other N atom(s) via a quasi H-N bond as they are spatially close enough for the charge densities to sufficiently overlap (Figure 8A), which further enhances the binding strength of H (Especially in the [N1] configuration of SV+3N, as H forms quasi H-N bonds with two other N atoms). However, if more H atoms were added in, they would be too squeezed within the small vacancy hole. Hence they become

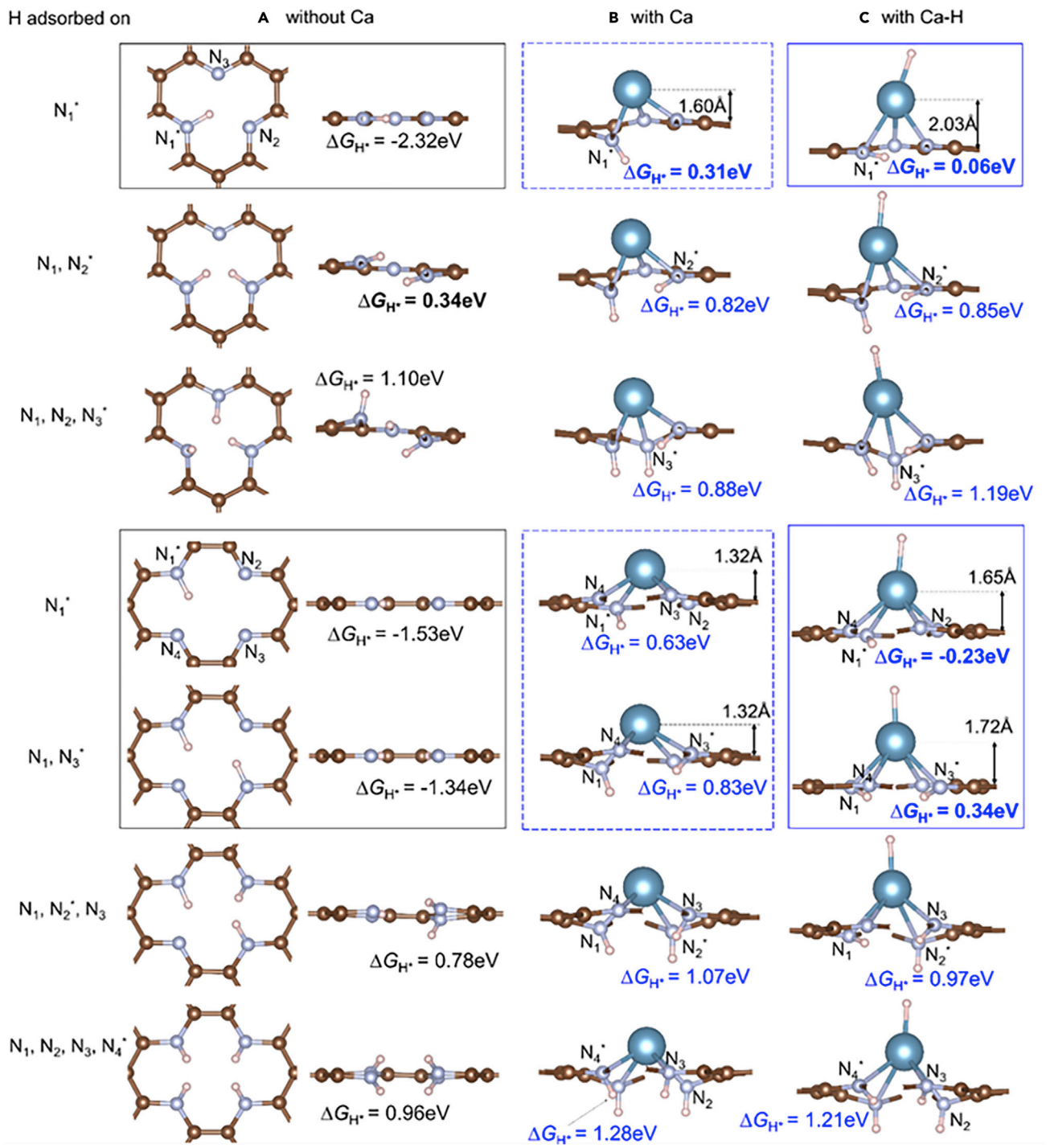

Figure 6. Atomic structure analysis and hydrogen adsorption

Atomic structures and ΔG_{H^*} values of H adsorption at each N-site of SV+3N and DV+4N (A) without Ca, (B) with a Ca single atom, and (C) with an extra H adsorbed onto Ca (In the side views some C atoms blocking N and H atoms from our view are not shown). Each ΔG_{H^*} value is for H adsorption onto the N atom indicated by *. When two H atoms are adsorbed onto DV+4N they prefer to adsorb at two N in diagonal positions [N_1, N_3] rather than neighboring positions [N_1, N_2], as the diagonal configuration is more stable due to longer separation between the two H* (Fujimoto and Saito, 2014). The structures in black boxes are planar, with very strong H binding (very negative ΔG_{H^*} values). Adsorbing one more H (below black boxes) or depositing a Ca atom (dashed blue boxes) significantly increases ΔG_{H^*} values to very positive values by changing N-H bond from sp^2-like to sp^3-like and breaks the charge density interaction between H and other N atoms. Further adsorbing an H onto Ca (blue boxes) reduces the influence of Ca to graphene structure, hence reduces ΔG_{H^*} to less positive values and makes them more suitable for HER.

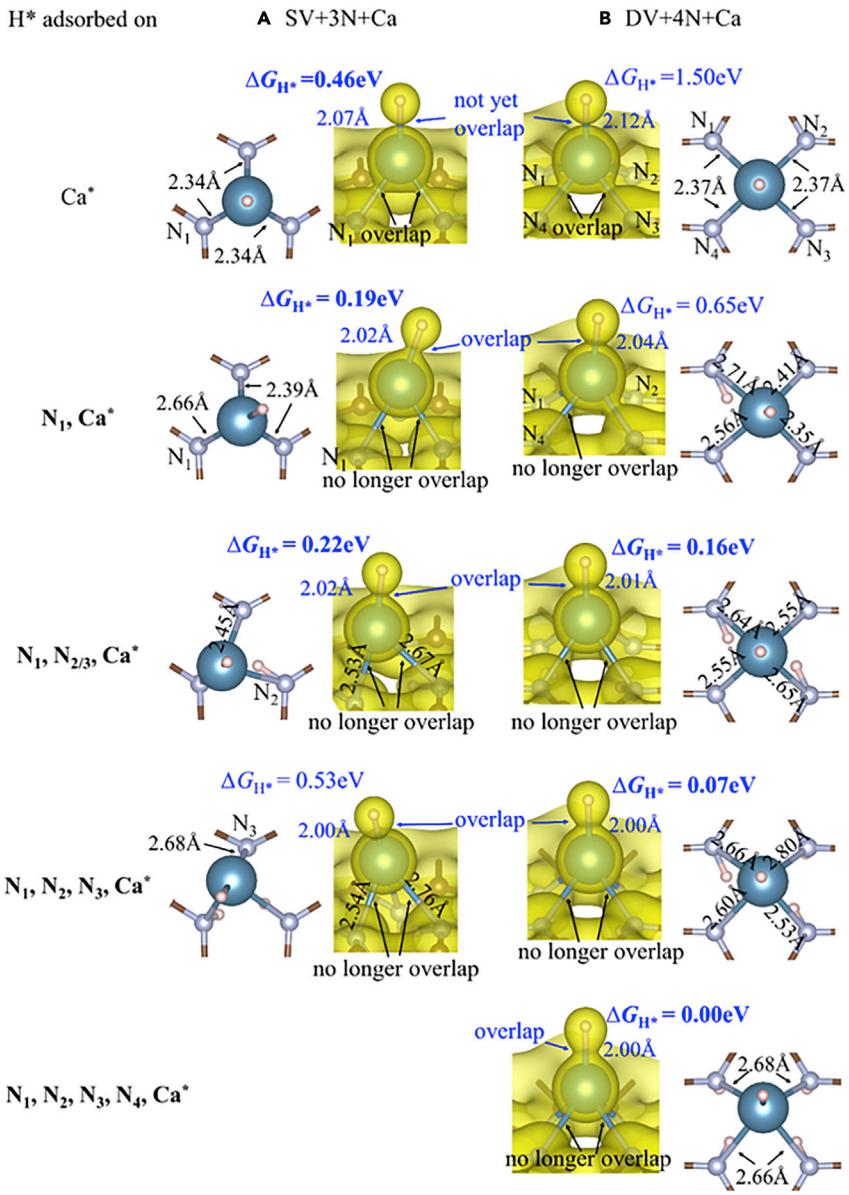

Figure 7. Atomic structure and charge density analysis

Atomic structures and charge densities of configurations with an H adsorbed on the Ca-site of (A) SV+3N + Ca and (B) DV+4N + Ca structures, and with various numbers of H adsorbed onto the N-sites. Charge density isosurfaces are at isovalues of 0.045 e/bohr^3 in (A) and 0.040 e/bohr^3 in (B), respectively. The ΔG_{H^*} for H adsorbed on Ca-sites is reduced to very good values by adsorbing H onto the N-sites.

out-of-plane due to Pauli repulsion (Figure 6A, below black boxes). Some N atoms also move out-of-plane. This changes the H-N bonding from sp^2-like toward more sp^3-like and also reduces the charge density interaction between H and other N atoms. Hence the H binding strength is significantly reduced.

When a Ca atom is deposited onto SV+3N or DV+4N, the Ca atom strongly binds to all the N atoms. This increases the CN of each H adsorbed N from three to four (Figure 6B) and changes the N-H bonding nature to sp^3-like. In addition, H is pushed out-of-plane substantially, losing quasi-bonding interaction with other N atoms (Figure 8B). This significantly reduces the H binding strength on N-sites. As a result, the corresponding ΔG_{H^*} values become quite positive, but with $|\Delta G_{H^*}|$ closer to 0 than in the structures without Ca (Figure 6B boxes vs Figure 6A boxes). This is one effect of Ca single atoms, namely reducing the H

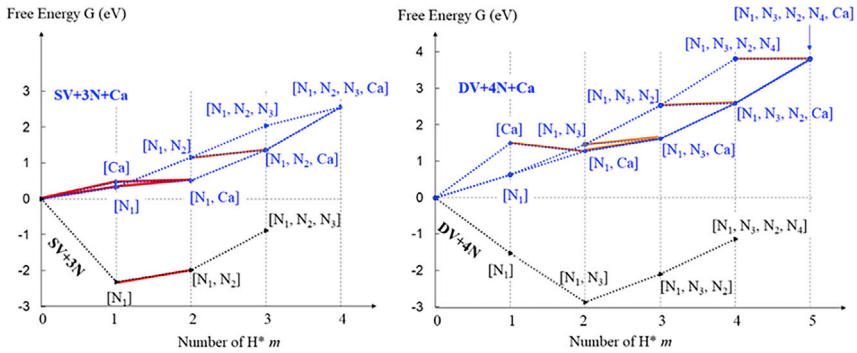

Scheme 1. Reaction energetics

Free energy G of various configurations involving m H adsorbed on the catalyst, for the SV+3N vs SV+3N + Ca and DV+4N vs DV+4N + Ca structures. To be consistent, G also involves free energy of the n-m H in H_2 phase, where n is the maximum number of H that could adsorb onto the catalyst (n = 3 for SV+3N, 4 for SV+3N + Ca and DV+4N, and 5 for DV+4N + Ca). Namely, G = G(catalyst + mH) $+\frac{n-m}{2}G(H_2)$. G values for configurations with m = 0 are set to 0. The G difference between two configurations connected by dashed lines represents the ΔG_{H^*} value of changing between these two configurations by adsorbing/desorbing an H. All ΔG_{H^*} values are also listed in Figures 6 and 7. H adsorption processes with $|\Delta G_{H^*}| < 0.5$ eV (small slope) are highlighted in red or orange.

binding strength on N-sites to better values for HER by changing the H-N bond nature to more sp^3-like and reducing the charge density interaction between H and other N atoms.

In fact, the Ca atom too significantly reduces the H binding strength at the N-site, making ΔG_{H^*} a bit too positive for HER (Figure 6B boxes). The influence of Ca could be slightly weakened by further adsorbing an H on top of Ca, which adjusts ΔG_{H^*} (of H adsorption on N) to less positive values, making the systems more suitable for HER (Figure 6C blue boxes). For example, the [$\mathbf{N_1}$*, Ca] configuration of SV+3N + Ca exhibits ΔG_{H^*} values of 0.06 eV, superior for catalyzing HER. Here the influence of Ca on the graphene structure is reduced because the H-Ca bond weakens Ca-N interactions, as can be seen by the increase of the Ca to graphene-plane distance (Figure 6C vs 6B). This makes the whole graphene structure deviate less from a 2D planar layer, hence allowing most of the N-H bonds to become less sp^3-like and more sp^2-like (Figure 6C vs 6B). The returning of the H toward the 2D planar layer also enhances the charge density interactions between H and other N atom(s) (Figure 8C vs 8B). Hence the overall H binding to N-sites is strengthened and becomes more suitable for HER.

For the four structures outside the boxes in Figure 6A, the H bindings are very weak because these H atoms are already repulsed out-of-plane by other H, even without a Ca deposition. Depositing a Ca atom makes slight differences to the H binding strength. Furthermore, adsorbing an H onto Ca also makes little change to the H binding strength on N-sites.

Besides the two effects discussed above, the Ca atom itself also serves as an H adsorption site with exceptional ΔG_{H^*} values. Our calculations predict that an H atom adsorbs on top of Ca, with ΔG_{H^*} values of 0.46 eV and 1.50 eV for SV+3N + Ca and DV+4N + Ca, respectively (Figure 7). The latter case has a weaker H-Ca bond because its Ca CN is higher. Although the two ΔG_{H^*} values are too positive for HER, they can be reduced to very good values by adsorbing H atoms onto the N-sites (Figure 7). *For example, for the [**N_1, Ca***] and [**N_1, N_2, Ca***] configurations of SV+3N + Ca, and the [**N_1, N_3, Ca***] configurations of DV+4N + Ca, ΔG_{H^*} are reduced to exceptional values for HER: 0.19, 0.22, and 0.16 eV, respectively.* However, this excludes the [$\mathbf{N_1}$, $\mathbf{N_2}$, $\mathbf{N_3}$, **Ca***] configuration of SV+3N + Ca, where ΔG_{H^*} is slightly increased compared to [**Ca***] configuration.

Adsorbing H on the N-sites can reduce the ΔG_{H^*} values of H adsorption on Ca sites, because the H-N bond weakens the N-Ca bonds, as can be seen by the N-Ca bond length increase (Figure 7 rows 2-5 compared to row 1). The weakening of N-Ca bonds is also reflected in the charge density plots in Figure 8. When there is no H adsorbed on any N we clearly see charge density overlap between Ca and the three/four N atoms. After adsorbing one or more H onto the N sites, most overlapping between Ca and N diminishes substantially. As a result, more valence electrons of Ca are involved to form a stronger Ca-H bond. Again, the

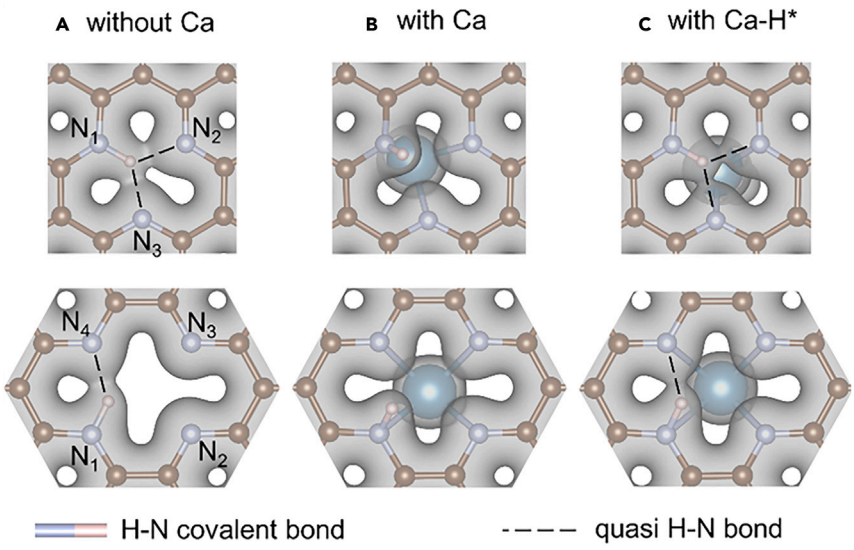

Figure 8. Charge density analysis

Charge densities of structures with one H adsorbed at the N_1-site of (top) SV+3N and (bottom) DV+4N for cases (A) without Ca, (B) with Ca, and (C) with an extra H adsorbed on Ca. The Ca atom and Ca-H are on the top side of graphene, while all charge density plots are viewed from the bottom side to better see the interaction between H and each N atom. All isosurfaces are at the same isovalue of 0.035 e/bohr^3. Moderate charge density overlap between H and an N atom (not covalently bonded to H) indicates a quasi H-N bond, as denoted by dashed lines. (A) and (C) involve one H-N covalent bond and 1 to 2 quasi H-N bonds. (B) involves no quasi H-N bonds because H is extensively out-of-plane.

strengthening of the Ca-H bond is reflected in both decreased Ca-H bond length and increased charge density overlap between Ca and H (Figure 7 row 2-5 compared to row 1).

In summary, we have explained three effects of Ca single atoms. First, the Ca atom makes H binding on N sites less stable by changing the H-N bonding nature more toward sp^3-like and reducing the charge density interaction between H and other N atoms. Secondly, the H-N binding is over-weakened by a Ca single atom. With an extra H adsorbed on top of Ca the H-N binding can be strengthened. Thirdly, the Ca atom itself serves as an H adsorption site, with the adsorption strength adjustable by H adsorbed onto N. The latter two effects both result in many H adsorption processes with perfect ΔG_{H^*} values. In particular, without Ca single atoms there are 7 unique processes of H adsorption and most of them have ΔG_{H^*} values that are either too negative or too positive. Depositing a single Ca atom generates 23 unique processes of H adsorption and many of them are better than the 7 processes in former situations for HER. Therefore, we conclude that the Ca single atom significantly enhances the HER activity of N-doped graphene.

Conclusion

Atomically confined calcium in NG (Ca_1-NG) was successfully synthesized as an efficient catalyst for electrocatalytic and photocatalytic hydrogen evolution. HADDF-STEM images and X-ray absorption spectroscopy analyses confirm the uniformly dispersed single Ca atoms on the NG substrate. Ca K-edge EXAFS fitting curves and DFT calculations indicate the Ca single-atoms are anchored in the pyridinic-N defects in graphene to form a Ca-N_3 structure. DFT calculations suggest that Ca atoms are trapped in SV+3N and DV+4N centers and Ca clustering is prevented. The high catalytic activity of Ca_1-NG for HER and PHE results from the Ca single-atoms in NG, which leads to multiple H adsorption configurations with very favorable ΔG_{H^*} values for HER. This research has pointed to a new approach for the development of high performance HER catalysts using non-transition metals.

Limitations of the study

Here we have revealed that atomically confined Ca in NG (Ca_1-NG) can effectively boost the electrocatalytic and photocatalytic HERs (EHE and PHE). Catalyst characterizations have shown that Ca single atoms anchored in NG can efficiently enhance the HER performance, improve the interfacial charge transfer, and

suppress the photo-generated charge recombination. However, one limitation of this study is that the loading concentration of single-atom Ca prepared by the current method is low. We will further improve the single-atom preparation method to increase the loading in our future work.

STAR★METHODS

Detailed methods are provided in the online version of this paper and include the following:

- KEY RESOURCES TABLE
- RESOURCE AVAILABILITY
  - Lead contact
  - Material availability
  - Data and code availability
- METHODS DETAILS
  - Synthesis of Ca_1-NG/CdS photocatalysts
  - Photocatalytic activity measurements
  - Electrochemical property measurements
  - Photoelectrochemical property measurements
  - XPS analyses
  - EXAFS fitting
  - Computational methods

SUPPLEMENTAL INFORMATION

Supplemental information can be found online at https://doi.org/10.1016/j.isci.2021.102728.

ACKNOWLEDGMENTS

This work was financially supported by the Natural Science Foundation of Shanghai (19ZR1420200), Science and Technology Commission of Shanghai Municipality (19DZ2271100), and Shanghai Committee of Science and Technology (17DZ2282800). The authors thank Prof. Song Hong from Beijing University of Chemical Technology for his help on the electron microscopy characterization at the atomic level. S.L. acknowledges the postdoc fellowship provided by Agency for Science Technology and Research (A*STAR) of Singapore. The computations in this paper were performed on the Odyssey cluster supported by the FAS Division of Science, Research Computing Group at Harvard University. S.L. also thanks Prof. Efthimios Kaxiras for helpful discussions.

AUTHOR CONTRIBUTIONS

W.Y. designed the research. J.S., Q.Z., and Q.W. performed the syntheses, most of the structural characterizations, electrochemical and photocatalytic tests. S.L. and W.C. performed DFT simulations. The paper was co-written by W.Y., S.L., and C.H. The research was supervised by W.Y. and Q.X. All authors discussed the results and comments on the manuscript.

DECLARATION OF INTERESTS

The authors declare no competing interests.

Received: February 22, 2021
Revised: May 24, 2021
Accepted: June 11, 2021
Published: July 23, 2021

SUPPORTING CITATIONS

The following reference appears in the Supplemental Information: Chen et al., 2019; Gopannagari et al., 2017; Hu et al., 2019; Irfan et al., 2019; Li et al., 2019a; Li et al., 2019b; Liu et al., 2020; Ran et al., 2017; Rangappa et al., 2020; Ruan et al., 2020; Sun et al., 2020; Wang et al., 2020; Ye et al., 2019; Zhang and Jin, 2019; Zhang et al., 2019; Zhang et al., 2020.

REFERENCES

Begouin, J.M., and Niggemann, M. (2013). Calcium-based Lewis acid catalysts. Chemistry *19*, 8030–8041.

Chen, X., Shen, S., Guo, L., and Mao, S.S. (2010). Semiconductor-based photocatalytic hydrogen generation. Chem. Rev. *110*, 6503–6570.

Chen, L., Xu, Y., and Chen, B. (2019). In situ photochemical fabrication of CdS/g-C_3N_4 nanocomposites with high performance for hydrogen evolution under visible light. Appl. Catal. B Environ. *256*, 117848.

Crimmin, M.R., Casely, I.J., and Hill, M.S. (2005). Calcium-mediated intramolecular hydroamination catalysis. J. Am. Chem. Soc. *127*, 2042–2043.

Dong, J., Wu, Q., Huang, C., Yao, W., and Xu, Q. (2018). Cost effective Mo rich Mo_2C electrocatalysts for the hydrogen evolution reaction. J. Mater. Chem. A *6*, 10028–10035.

Fei, H., Dong, J., Arellano-Jimenez, M.J., Ye, G., Dong Kim, N., Samuel, E.L., Peng, Z., Zhu, Z., Qin, F., Bao, J., et al. (2015). Atomic cobalt on nitrogen-doped graphene for hydrogen generation. Nat. Commun. *6*, 8668.

Ferrari, A.C., and Basko, D.M. (2013). Raman spectroscopy as a versatile tool for studying the properties of graphene. Nat. Nanotechnol. *8*, 235–246.

Fujimoto, Y., and Saito, S. (2014). Hydrogen adsorption and anomalous electronic properties of nitrogen-doped graphene. J. Appl. Phys. *115*, 153701.

Gao, G., Jiao, Y., Ma, F., Jiao, Y., Waclawik, E., and Du, A. (2015). Metal-free graphitic carbon nitride as mechano-catalyst for hydrogen evolution reaction. J. Catal. *332*, 149–155.

Gerken, J.B., Shaner, S.E., Massé, R.C., Porubsky, N.J., and Stahl, S.S. (2014). A survey of diverse earth abundant oxygen evolution electrocatalysts showing enhanced activity from Ni–Fe oxides containing a third metal. Energy Environ. Sci. *7*, 2376–2382.

Gopannagari, M., Kumar, D.P., Reddy, D.A., Hong, S., Song, M.I., and Kim, T.K. (2017). In situ preparation of few-layered WS_2 nanosheets and exfoliation into bilayers on CdS nanorods for ultrafast charge carrier migrations toward enhanced photocatalytic hydrogen production. J. Catal. *351*, 153–160.

Grimme, S., Antony, J., Ehrlich, S., and Krieg, H. (2010). A consistent and accurate ab initio parametrization of density functional dispersion correction (DFT-D) for the 94 elements H-Pu. J. Chem. Phys. *132*, 154104.

Harder, S. (2010). From limestone to catalysis: application of calcium compounds as homogeneous catalysts. Chem. Rev. *110*, 3852–3876.

Harder, S., and Brettar, J. (2006). Rational design of a well-defined soluble calcium hydride complex. Angew. Chem. Int. Ed. *45*, 3474–3478.

Hill, M.S., Liptrot, D.J., and Weetman, C. (2016). Alkaline earths as main group reagents in molecular catalysis. Chem. Soc. Rev. *45*, 972–978.

Hu, J.C., Sun, S., Li, M.D., Xia, W., Wu, J., Liu, H., and Wang, F. (2019). A biomimetic self-assembled cobaloxime@CdS/rGO hybrid for boosting photocatalytic H_2 production. Chem. Commun. *55*, 14490–14493.

Irfan, R.M., Tahir, M.H., Khan, S.A., Shaheen, M.A., Ahmed, G., and Iqbal, S. (2019). Enhanced photocatalytic H_2 production under visible light on composite photocatalyst (CdS/NiSe nanorods) synthesized in aqueous solution. J. Colloid Interf. Sci. *557*, 1–9.

Jiang, K., Siahrostami, S., Akey, A.J., Li, Y., Lu, Z., Lattimer, J., Hu, Y., Stokes, C., Gangishetty, M., Chen, G., et al. (2017). Transition-metal single atoms in a graphene shell as active centers for highly efficient artificial photosynthesis. Chem *3*, 950–960.

Kaiser, S.K., Chen, Z., Faust Akl, D., Mitchell, S., and Perez-Ramirez, J. (2020). Single-atom catalysts across the periodic table. Chem. Rev. *120*, 11703–11809.

Kresse, G., and Furthmüller, J. (1996). Efficient iterative schemes for ab initio total-energy calculations using a plane-wave basis set. Phys. Rev. B *54*, 11169–11186.

Kweon, D.H., Okyay, M.S., Kim, S.J., Jeon, J.P., Noh, H.J., Park, N., Mahmood, J., and Baek, J.B. (2020). Ruthenium anchored on carbon nanotube electrocatalyst for hydrogen production with enhanced Faradaic efficiency. Nat. Commun. *11*, 1278.

Lee, H., Ihm, J., Cohen, M.L., and Louie, S.G. (2009). Calcium-decorated carbon nanotubes for high-capacity hydrogen storage: first-principles calculations. Phys. Rev. B *80*, 115412.

Li, C., Du, S., Wang, H., Naghadeh, S.B., Allen, A.L., Lin, X., Li, G., Liu, Y., Xu, H., He, C., et al. (2019a). Enhanced visible-light-driven photocatalytic hydrogen generation using $NiCo_2S_4$/CdS nanocomposites. Chem. Eng. J. *378*, 122089.

Li, N., Ding, Y., Wu, J., Zhao, Z., Li, X., Zheng, Y.Z., Huang, M., and Tao, X. (2019b). Efficient, full spectrum-driven H_2 evolution Z-scheme Co_2P/CdS photocatalysts with Co-S bonds. ACS Appl. Mater. Inter. *11*, 22297–22306.

Lin, Y.-C., Teng, P.-Y., Yeh, C.-H., Koshino, M., Chiu, P.-W., and Suenaga, K. (2015). Structural and chemical dynamics of pyridinic-nitrogen defects in graphene. Nano Lett. *15*, 7408–7413.

Lin, C.-Y., Zhang, L., Zhao, Z., and Xia, Z. (2017). Design principles for covalent organic frameworks as efficient electrocatalysts in clean energy conversion and green oxidizer production. Adv. Mater. *29*, 1606635–1606637.

Liu, S., Li, Z., Wang, C., Tao, W., Huang, M., Zuo, M., Yang, Y., Yang, K., Zhang, L., Chen, S., et al. (2020). Turning main-group element magnesium into a highly active electrocatalyst for oxygen reduction reaction. Nat. Commun. *11*, 938.

Luo, M., Yao, W., Huang, C., Wu, Q., and Xu, Q. (2015). Shape effects of Pt nanoparticles on hydrogen production via Pt/CdS photocatalysts under visible light. J. Mater. Chem. A *3*, 13884–13891.

Mathew, S., Ani Joseph, S., Radhakrishnan, P., Nampoori, V.P., and Vallabhan, C.P. (2011). Shifting of fluorescence peak in CdS nanoparticles by excitation wavelength change. J. Fluoresc. *21*, 1479–1484.

Naumkin, A.V., Kraut-Vass, A., Gaarenstroom, S.W., and Powell, C.J. (2012). X-ray Photoelectron Spectroscopy Database (NIST).

Nørskov, J.K., Bligaard, T., Logadottir, A., Kitchin, J.R., Chen, J.G., Pandelov, S., and Stimming, U. (2005). Trends in the exchange current for hydrogen evolution. J. Electrochem. Soc. *152*, J23–J26.

Perdew, J.P., Burke, K., and Ernzerhof, M. (1996). Generalized gradient approximation made simple. Phys. Rev. Lett. *77*, 3865–3868.

Ran, J., Gao, G., Li, F.T., Ma, T.Y., Du, A., and Qiao, S.Z. (2017). Ti_3C_2 MXene co-catalyst on metal sulfide photo-absorbers for enhanced visible-light photocatalytic hydrogen production. Nat. Commun. *8*, 13907.

Rangappa, A.P., Kumar, D.P., Gopannagari, M., Reddy, D.A., Hong, Y., Kim, Y., and Kim, T.K. (2020). Highly efficient hydrogen generation in water using 1D CdS nanorods integrated with 2D SnS_2 nanosheets under solar light irradiation. Appl. Surf. Sci. *508*, 144803.

Ruan, D., Fujitsuka, M., and Majima, T. (2020). Exfoliated Mo_2C nanosheets hybridized on CdS with fast electron transfer for efficient photocatalytic H_2 production under visible light irradiation. Appl. Catal. B Environ. *264*, 118541.

Shi, Y., Lei, X.F., Xia, L.G., Wu, Q., and Yao, W.F. (2020). Enhanced photocatalytic hydrogen production activity of CdS coated with Zn-anchored carbon layer. Chem. Eng. J. *393*, 124751.

Sun, K., Shen, J., Yang, Y., Tang, H., and Lei, C. (2020). Highly efficient photocatalytic hydrogen evolution from 0D/2D heterojunction of FeP nanoparticles/CdS nanosheets. Appl. Surf. Sci. *505*, 144042.

Veamatahau, A., Jiang, B., Seifert, T., Makuta, S., Latham, K., Kanehara, M., Teranishi, T., and Tachibana, Y. (2015). Origin of surface trap states in CdS quantum dots: relationship between size dependent photoluminescence and sulfur vacancy trap states. Phys. Chem. Chem. Phys. *17*, 2850–2858.

Wang, Y., Mao, J., Meng, X., Yu, L., Deng, D., and Bao, X. (2019). Catalysis with two-dimensional materials confining single atoms: concept, design, and applications. Chem. Rev. *119*, 1806–1854.

Wang, L., Zhou, H., Zhang, H., Song, Y., Zhang, H., Luo, L., Yang, Y., Bai, S., Wang, Y., and Liu, S. (2020). Facile in situ formation of a ternary 3D $ZnIn_2S_4$-MoS_2 microsphere/1D CdS nanorod heterostructure for high-efficiency visible-light

photocatalytic H_2 production. Nanoscale *12*, 13791–13800.

Wu, X., Zhao, L., Jin, J., Pan, S., Li, W., Jin, X., Wang, G., Zhou, M., and Frenking, G. (2018). Observation of alkaline earth complexes $M(CO)_8$ (M = Ca, Sr, or Ba) that mimic transition metals. Science *361*, 912–916.

Wu, J., Xiong, L., Zhao, B., Liu, M., and Huang, L. (2019). Densely populated single atom catalysts. Small Methods *4*, 1900540.

Xu, J., Yan, X., Qi, Y., Fu, Y., Wang, C., and Wang, L. (2019). Novel phosphidated MoS_2 nanosheets modified CdS semiconductor for an efficient photocatalytic H_2 evolution. Chem. Eng. J. *375*, 122053.

Yang, S., Tak, Y.J., Kim, J., Soon, A., and Lee, H. (2017). Support effects in single-atom platinum catalysts for electrochemical oxygen reduction. ACS Catal. *7*, 1301–1307.

Yao, J., Zheng, Y., Jia, X., Duan, L., Wu, Q., Huang, C., An, W., Xu, Q., and Yao, W. (2019). Highly active Pt_3Sn{110}-Excavated nanocube cocatalysts for photocatalytic hydrogen production. ACS Appl. Mater. Inter. *11*, 25844–25853.

Ye, L., Ma, Z., Deng, Y., Ye, Y., Li, W., Kou, M., Xie, H., Zhikun, X., Zhou, Y., Xia, D., and Wong, P.K. (2019). Robust and efficient photocatalytic hydrogen generation of ReS_2/CdS and mechanistic study by on-line mass spectrometry and in situ infrared spectroscopy. Appl. Catal. B Environ. *257*, 117897.

Yoon, M., Yang, S., Hicke, C., Wang, E., Geohegan, D., and Zhang, Z. (2008). Calcium as the superior coating metal in functionalization of carbon fullerenes for high-capacity hydrogen storage. Phys. Rev. Lett. *100*, 206806.

Zhang, Y., and Jin, Z. (2019). Effective electron-hole separation over a controllably constructed WP/UiO-66/CdS heterojunction to achieve efficiently improved visible-light-driven photocatalytic hydrogen evolution. Phys. Chem. Chem. Phys. *21*, 8326–8341.

Zhang, L., Zhang, H., Wang, B., Huang, X., Ye, Y., Lei, R., Feng, W., and Liu, P. (2019). A facile method for regulating the charge transfer route of WO_3/CdS in high-efficiency hydrogen production. Appl. Catal. B Environ. *244*, 529–535.

Zhang, B., Chen, C., Liu, J., Qiao, W., Zhao, J., Yang, J., Yu, Y., Chen, S., and Qin, Y. (2020). Simultaneous Ni nanoparticles decoration and Ni doping of CdS nanorods for synergistically promoting photocatalytic H_2 evolution. Appl. Surf. Sci. *508*, 144869.

Zhao, Q., Yao, W., Huang, C., Wu, Q., and Xu, Q. (2017). Effective and durable Co single atomic cocatalysts for photocatalytic hydrogen production. ACS Appl. Mater. Inter. *9*, 42734–42741.

Zhao, Q., Sun, J., Li, S., Huang, C., Yao, W., Chen, W., Zeng, T., Wu, Q., and Xu, Q. (2018). Single nickel atoms anchored on nitrogen-doped graphene as a highly active cocatalyst for photocatalytic H_2 evolution. ACS Catal. *8*, 11863–11874.

Zheng, Y., Dong, J., Huang, C., Xia, L., Wu, Q., Xu, Q., and Yao, W. (2020). Co-doped Mo-Mo_2C cocatalyst for enhanced g-C_3N_4 photocatalytic H_2 evolution. Appl. Catal. B Environ. *260*, 118220.

Zhu, B., Qiu, K., Shang, C., and Guo, Z. (2015). Naturally derived porous carbon with selective metal- and/or nitrogen-doping for efficient CO_2 capture and oxygen reduction. J. Mater. Chem. A *3*, 5212–5222.

Zhu, J., Hu, L., Zhao, P., Lee, L.Y.S., and Wong, K.Y. (2020a). Recent advances in electrocatalytic hydrogen evolution using nanoparticles. Chem. Rev. *120*, 851–918.

Zhu, Y., Chen, J., Shao, L., Xia, X., Liu, Y., and Wang, L. (2020b). Oriented facet heterojunctions on CdS nanowires with high photoactivity and photostability for water splitting. Appl. Catal. B Environ. *268*, 118744.

Zhuo, H.Y., Zhang, X., Liang, J.X., Yu, Q., Xiao, H., and Li, J. (2020). Theoretical understandings of graphene-based metal single-atom catalysts: stability and catalytic performance. Chem. Rev. *120*, 12315–12341.

STAR★METHODS

KEY RESOURCES TABLE

REAGENT or RESOURCE	SOURCE	IDENTIFIER
Chemicals, peptides, and recombinant proteins		
cadmium sulfide	Sinopharm Chemical Reagent (Shanghai, China)	CAS:1306-23-6
anhydrous calcium chloride	Sinopharm Chemical Reagent (Shanghai, China)	CAS:10043-52-4
concentrated sulfuric acid	Sinopharm Chemical Reagent (Shanghai, China)	CAS:7664-93-9
potassium permanganate	Sinopharm Chemical Reagent (Shanghai, China)	CAS:7722-64-7
graphite powder	Macklin Reagent Co., Ltd	CAS:7782-42-5
sodium nitrate	Macklin Reagent Co., Ltd	CAS:7631-99-4
30% hydrogen peroxide	Macklin Reagent Co., Ltd	CAS:7722-84-1
ammonium sulfite monohydrate	Aladdin Reagent Co., Ltd	CAS:7783-11-1
Software and algorithms		
Vienna Ab-initio Simulation Package (VASP)	Tongji University	http://software.tongji.edu.cn/Home/IndexPage
Other		
JEOL JEM-2100F/HR transmission electron microscope	JEOL (BEIJING) CO., LTD.	http://www.jeol.com.cn/product/detail/617
JEOL JEM-ARM200F microscope	JEOL (Beijing) Co., Ltd.	http://www.jeol.com.cn/product/detail/402
BRUKER-D8 X-ray diffractometer	Bruker (Beijing) Scientific Technology Co. Ltd.	https://www.bruker.com/zh/products-and-solutions/diffractometers-and-scattering-systems/x-ray-diffractometers/d8-advance-family/d8-advance-eco.html
Lab RAM high-resolution (HR) evolution Raman spectrometer	HORIBA Jobin Yvon	https://www.horiba.com/cn/scientific/markets-industries/display-technologies/
ESCALAB250 spectrometer	Thermofisher Scientific(China)Co.,Ltd.	https://www.thermofisher.cn/order/catalog/product/SID-10148252?SID=srch-hj-ESCALAB250%20spectrometer#/SID-10148252?SID=srch-hj-ESCALAB250%20spectrometer
Inductively coupled plasma optical emission spectrometer (ICP-OES) Optima 8000	PerkinElmer Management (Shanghai) Co., Ltd	https://www.perkinelmer.com.cn/searchresult?searchName=Optima%25208000&_csrf=f3b614e8-0109-41be-a294-dfb37e7310da
Fluorescence Detector (RF-10A, Shimadzu, Japan)	Shimadzu (Japan) Co., Ltd.	https://www.shimadzu.com.cn/an/gc/index.html
Edinburgh FLS9800	Edinburgh Instruments Ltd.	https://www.selectscience.net/companies/edinburgh-instruments-ltd/?compID=7445
Nicolet iS10 (Thermo Fisher, USA) infrared spectrometer	Thermofisher Scientific(China)Co.,Ltd.	https://www.thermofisher.cn/cn/zh/home.html
beamline XAFCA	Singapore Synchrotron Light Source (SSLS)	https://lightsources.org/cms/?pid=1000130

RESOURCE AVAILABILITY

Lead contact

Further information and requests for resources should be directed to and will be fulfilled by the lead contact, Weifeng Yao (yaoweifeng@shiep.edu.cn).

Material availability

This study did not generate new unique reagents.

Data and code availability

This study did not generate any unique datasets or code.

METHODS DETAILS

Synthesis of Ca_1-NG/CdS photocatalysts

Graphene oxide (GO) was synthesized using the traditional Hummer method. In detail, 2.000 g of graphite powder, 1.000 g of $NaNO_3$ and 46 ml of H_2SO_4 were added into a beaker soaked in an ice bath and well stirred. Under stirring, then 6.000 g of $KMnO_4$ powder was slowly added to the above mixture for 10 minutes. The mixture was then heated to 35 °C for 30 minutes. Next, after adding 92 mL of deionized water the mixture was heated to 98 °C. At the same time 60 mL 30% H_2O_2 was slowly added to the mixture to prevent graphene oxidation. Finally, the mixture was centrifuged and washed repeatedly with deionized water. A golden yellow suspension was obtained by dispersing the obtained precipitate in water and then filtering. GO was obtained by freeze-drying the golden yellow suspension.

Single calcium atom anchored nitrogen doped graphene (Ca_1-NG) was synthesized via an impregnation method, followed by a calcination process under NH_3 atmosphere. The synthesis details are as follows: 100.0 mg of GO and 1.0 mg of $CaCl_2$ were dispersed into 50 mL deionized water. The mixture was sonicated for 4 hours to form a uniformly dispersed suspension. Then liquid nitrogen was added into the suspension to form a solid mixture, followed by freeze-drying for 24 hours. The resulting product was named Ca-GO. Finally, Ca-GO powder was calcinated under NH_3 at 750 °C for 1 hour to synthesize Ca_1-NG. The method for the preparation of CaO-NG was adopted from a similar method reported, except that in this research it was calcined in air at 750 °C for 1h before calcining under NH_3. The prepared Ca_1-NG (or CaO-NG) was then coupled with CdS using an impregnation method. Briefly, certain amounts of Ca_1-NG (or CaO-NG) and CdS were added into an ethanol solution. Then the mixture was stirred at room temperature until the ethanol had completely evaporated. The obtained dark yellow powder was Ca_1-NG/CdS (or CaO-NG/CdS).

Photocatalytic activity measurements

Photocatalytic hydrogen evolution activity was measured at 420 nm wavelength. 5.0 mg prepared catalysts were dispersed in 10 mL 1.0 M aqueous $(NH_4)_2SO_3$ solution. The solution was degassed with N_2 for 1 h to remove dissolved oxygen before being irradiated with a single-wavelength (420 nm) light-emitting diode (LED) monochromatic lamp (CEL-LED 100). The H_2 evolution volume was analyzed via an online gas chromatograph (Techcomp Limited Co., GC7890II) equipped with a thermal conductivity detector. Ultra-pure nitrogen was used as a carrier gas.

The apparent quantum efficiency (AQE) was measured and calculated according to the following equation:

$$AQE(\%) = \frac{number\ of\ reacted\ electrons}{number\ of\ incident\ photons} \times 100\%$$
$$= \frac{\text{number of evolved } H_2 \text{molecules x 2}}{\text{number of incident photons}} \times 100\%$$
$$= \frac{2 \times n_{H_2}}{I_0 \times t} \times 100\%$$

where n_{H_2} is the mole numbers for hydrogen evolution from t = 0 to time *t*. and I_0 is the Einstein of incident photons per second measured at λ = 420 nm.

Electrochemical property measurements

Electrochemical properties of catalysts were measured using a CHI 660E electrochemical workstation in a standard three-electrode cell. 5.0 mg catalysts were dispersed in a solution consisting of 500 μL water, 500 μL ethanol and 80 μL 5.0 wt.% Nafion solution. The above mixture was then sonicated for 1 h to form a homogeneous suspension. A working electrode was prepared by dropping 5 μL of the suspension onto the surface of a glassy carbon electrode (GCE), which was then dried in air. The electrode surface area is 0.07 cm^2 with 0.265 mg cm^{-2} catalyst loading density. A saturated calomel electrode and a Pt foil were used as the reference electrode and the counter electrode, respectively. Linear-sweep voltammograms (LSV) were carried out at a scan rate of 2 mV S^{-1} in two electrolytes: one was a 0.5 M H_2SO_4 aqueous solution, and the other was a 1.0 M $(NH_4)_2SO_3$ aqueous solution.

The turnover frequency (TOF) values were calculated according to the Equation below:

$$TOF = j \times A\ (2F \times n)$$

Where, j is the current density obtained at overpotential of 100 mV, A is the surface area of the electrode, F is the Faraday efficiency (96,485 mol^{-1}), and n is the mole numbers of catalysts deposited onto electrodes.

Cyclic voltammetry (CV) measurements were performed with scanning rates from 20 to 100 mV s^{-1} and potential ranges from 0.00 - 0.10 V (vs. RHE) in a 0.5 M H_2SO_4 solution. Double-layer capacitances (C_{dl}) were estimated based on current density variation as a linear function of scan rate. $\Delta j = (j_a - j_c)/2$ was obtained at 50 mV vs. RHE. The electrochemically active surface area (ECSA) was determined by the double layer capacitance (C_{dl}). The following equation was used to calculate ECSA:

$$ECSA\ (cm^2) = C_{dl}/C_s$$

The specific capacitance (C_s) of a flat surface is usually in the range of 20 ~ 60 μF cm^{-2}. We assumed C_s was 40 μF cm^{-2} in the calculation of the ECSA.

The ECSA of 20 wt.% Pt/C was calculated using the under-potential deposition hydrogen (UPD-H) adsorption/desorption voltammetry based on the following equation:

$$ECSA(cm^2) = \frac{0.5 \times S_H/v}{0.21\ (mC \cdot cm^{-2})}$$

Where S_H was the integral area of the adsorption/desorption region for H atoms (0.05 V–0.40 V), which was marked red in Figure S5, v is the scan rate.

Mott–Schottky method. In this research, we also estimated the CB potentials of Ca_1-NG and CdS using the Mott–Schottky method. As shown in Figure S16, the slopes of the Mott–Schottky plots for CdS and Ca_1-NG are greater than 0.00, suggesting that CdS and Ca_1-NG are both n-type semiconductors. Their flat band potentials (E_{fb}) are determined to be −0.58 V and −0.43 V (vs. SCE) for CdS and Ca_1-NG, respectively. In general, the CB edge potential (E_{CB}) is more negative by about −0.10 or −0.20 V than the E_{fb} for the n-type semiconductors. Therefore, the E_{CB} for CdS and for Ca_1-NG are −0.78 V and −0.63 V (vs. SCE), that is −0.54 V and −0.39 V (vs. NHE) (normal hydrogen electrode). This result indicates that under light irradiation, photogenerated electrons in CdS can migrate from CdS to Ca_1-NG at the heterojunction interfaces between Ca_1-NG and CdS.

Photoelectrochemical property measurements

Photoelectrochemical properties of catalysts were measured using a CHI 660E electrochemical workstation in a typical three-electrode system. The working electrode was prepared by dropping 50 μL of photocatalyst suspension onto the surface of a fluorine-doped tin oxide (FTO) conducting glass support with an area of 1.0 × 1.0 cm^2 and then dried in air. An Ag/AgCl and a Pt foil were used as the reference electrode and the counter electrode, respectively. 0.1 M Na_2SO_4 aqueous solution was used as the electrolyte, which was purged with N_2 to remove dissolved O_2. The light source was a single-wavelength (420 nm) LED monochromatic lamp, which was identical to the light source for photocatalytic H_2 evolution.

XPS analyses

XPS analyses were performed using an ESCALAB250 spectrometer equipped with a monochromatized Al Kα (1486.6 eV) source. The survey spectra were recorded in a 0.5 eV incremental with a pass energy of 140

eV. Detailed scans spectra were recorded in a 0.1 eV incremental with a pass energy of 140 eV. The elemental spectra were all corrected with respect to C1s peaks at 284.8 eV.

EXAFS fitting

To verify the above EXAFS results a least-squares curve fitting analysis was carried out for the first coordination shell spreading from 1.5 to 2.5 Å. All backscattering paths were calculated based on the structures provided by ab initio simulations. The energy shift (ΔE) was constrained for scatters at the same level. The path length R, coordination number (CN), and Debye–Waller factors σ^2 were left as free parameters. The fit was completed in R space with k range of 3.5–12.6 $Å^{-1}$ and k^2 weight.

Computational methods

All structures are calculated using density functional theory (DFT) implemented in the Vienna Ab-initio Simulation Package (VASP) (Kresse and Furthmüller, 1996). The exchange-correlation interaction is described by generalized gradient approximation (GGA) with the Perdew-Burke-Ernzerhof (PBE) functional (Perdew et al., 1996). The Ca_sv pseudopotential is used. The vdW interaction is considered by using the DFT-D3 method (Grimme et al., 2010) and spin-polarization effect is included. The electron wavefunctions are expanded using plane waves with an energy cutoff of 400 eV. Slab model is used for all calculations with a fixed cell thickness of 15 Å to ensure sufficient vacuum space. All structures are relaxed until all final residual forces on the atoms are smaller than 0.005 eV/Å. They are built from a graphene unit cell with lattice constant of 2.467 Å, as relaxed using the above parameters with a *k*-point mesh of 12 × 12×1. A supercell of 4 × 4×1 and *k*-mesh of 3 × 3×1 are employed for all structures.

ΔG_{H^*} includes three parts: the difference in electronic energy ΔE_H, the difference in zero point energy ΔE_{ZPE}, and the difference in entropy $T\Delta S_H$

$$\Delta G_{H^*} = \Delta E_{H^*} + \Delta E_{ZPE} - T\Delta S_{H^*}. \quad \text{(Equation 1)}$$

All the differences are between H in the adsorbed phase (H*) and in the gas phase (H_2). The vibrational frequency in H_2 is much higher than in H* phase, so ΔS_H mainly results from the H_2 molecule, namely, $T\Delta S_H \sim 0.5 \times TS_{H2} \sim 0.205$ eV at the standard condition (300 K, 1 bar) (Nørskov et al., 2005). The difference in zero point energy is usually very small. For example, ΔE_{ZPE} is around 0.02 eV for H adsorbed onto the double-coordinated N of graphitic-C_3N_4 (Gao et al., 2015) and around 0.035eV for H adsorbed onto Cu (111) surface (Nørskov et al., 2005). Here, we use these two values for H adsorbed on pyridinic-N and Ca single atom, respectively. In particular, we use

$$\Delta G_{H^*} = \Delta E_{H^*} + 0.23 \text{ eV for H adsorbed on pyridinic-N} \quad \text{(Equation 2)}$$

$$\Delta G_{H^*} = \Delta E_{H^*} + 0.24 \text{ eV for H adsorbed on Ca} \quad \text{(Equation 3)}$$

The major contribution to ΔG_{H^*} is the H adsorption energy, calculated as

$$\Delta E_{H^*} = E(\text{catalyst} + m\text{H}) - E(\text{catalyst}+(m\text{-}1)\text{H}) - 0.5 \times E(H_2), \quad \text{(Equation 4)}$$

where E(catalyst + mH) and E(catalyst+(m-1)H) refer to the total energies of the catalytic system with and without the adsorbed H that we are studying; $E(H_2)$ is the total energy of a gas phase H_2 molecule. These three structures are all with the same supercell size and sufficiently relaxed. When more than one H is adsorbed onto the structure we consider the adsorption of H atoms one by one. In other words, when we consider the m^{th} H atom, we use the structure with m-1 H atoms as the reference system.

Similarly to defining the H adsorption energy in Equation (4), we define the Ca adsorption energy as

$$\Delta E_{Ca} = E_{NG+Ca} - E_{NG} - E_{isolated\_Ca\_atom} \quad \text{(Equation 5)}$$

where E_{NG+Ca} and E_{NG} refer to the total energies of the N-doped graphene (NG) with or without Ca adsorption, and $E_{isolated\_Ca\_atom}$ is the total energy of an isolated single Ca atom.